Replacement of microglia by brain-engrafted macrophages provide long term protection against brain irradiation and concussive injury

Xi Feng[1,2], Elma S. Frias[1,2], Maria S. Paladini[1,2], David Chen[1,2,3], Zoe Boosalis[1,2],McKenna Becker[1,2], Sonali Gupta[1,2], Sharon Liu[3], Nalin Gupta[3,6,7] and Susanna Rosi[1,2,3,4,5*]

[1] Brain and Spinal Injury Center
[2] Department of Physical Therapy and Rehabilitation Science
[3] Department of Neurological Surgery
[4] Weill Institute for Neuroscience
[5] Kavli Institute of Fundamental Neuroscience
[6] Brain Tumor Research Center
[7] Department of Pediatrics
University of California San Francisco

* Corresponding Author
Susanna Rosi Ph.D.: Susanna.Rosi@ucsf.edu
1001 Potrero Ave, Building 1, Room 101, Zuckerberg San Francisco General Hospital
Department of Physical Therapy and Rehabilitation Science, University of California, San Francisco, San Francisco, CA 94110

Running Title: monocyte-derived macrophages protects against brain injury

Keywords: microglia, brain engrafted macrophages, cognition, brain irradiation, CSF-1R inhibitor

Abstract

Brain resident microglia have a distinct origin compared to macrophages in other organs. Under physiological conditions, microglia are maintained by self-renewal from the local pool, independent of hematopoietic progenitors. Pharmacological depletion of microglia during therapeutic whole-brain irradiation prevents synaptic loss and long-term recognition memory deficits but the mechanisms behind these protective effects are unknown. Here we demonstrate that after a combination of therapeutic whole-brain irradiation and microglia depletion, macrophages originating from circulating monocytes engraft into the brain and replace the microglia pool. Comparisons of transcriptomes reveal that brain-engrafted macrophages have an intermediate phenotype that resembles both monocytes and embryonic microglia. Brain-engrafted macrophages display reduced phagocytic activity for synaptic compartments compared to microglia from normal brains in response to a secondary concussive brain injury. In addition to sparing mice from brain radiotherapy-induced long-term cognitive deficits, replacement of microglia by brain-engrafted macrophages can prevent concussive injury-induced memory loss. These results demonstrate the long-term functional role of brain-engrafted macrophages as a possible therapeutic tool against radiation-induced cognitive deficits.

43

44 **Introduction**

45 Brain resident microglia are the innate immune cells of the central nervous system (CNS).
46 Arisen from the yolk sac during embryonic development, microglia actively survey the
47 environment to maintain normal brain functions [1, 2]. Under physiological conditions, microglia are
48 maintained solely by self-renewal from the local pool [3]. Following brain injury and other
49 pathological conditions, microglia become activated and play a central role in the clearance of
50 cellular debris, but if not controlled this process can result in aberrant synaptic engulfment [4-7].
51 Temporary depletion of microglia can be achieved by using pharmacologic inhibitors of the
52 colony-stimulating factor 1 receptor (CSF-1R) [8]. In the normal brain, treatment with CSF-1R
53 inhibitors (CSF-1Ri) can deplete up to 99% of microglia without causing detectable changes to
54 cognitive functions [8, 9]. Full repopulation occurs within 14 days of inhibitor withdrawal and the
55 repopulated microglia are morphologically and functionally identical to the microglia in naïve
56 brains [9]. Microglia depletion and repopulation by local progenitors has been shown to be beneficial
57 for disease- ,injury- , and age-associated neuropathological and behavioral conditions[10-15].
58 However, the mechanisms for these protective effects are unknown.

59 Whole-brain radiotherapy (WBRT), delivered in multiple fractions, is routinely used to treat
60 patients with brain tumors. It is estimated that more than 200,000 patients receive WBRT yearly
61 in the US alone [16]. While it is effective in improving intracranial tumor control, WBRT leads to
62 deterioration of patients' cognitive functions and quality of life [17-19]. Currently, there is no treatment
63 available to prevent or mitigate these adverse effects. Previous studies demonstrated that WBRT
64 causes deleterious effects to the CNS microenvironment by a number of mechanisms including
65 apoptosis of neural progenitor cells, disruption of the blood-brain barrier, activation of microglia
66 and accumulation of peripherally derived macrophages [20-25]. We and others have reported that
67 depletion of microglia during or shortly after brain irradiation in animal models can prevent loss of

68 dendritic spines in hippocampal neurons and cognitive impairments that develop at later time
69 points [12-14]. These reports suggest that microglial plays a critical role in inducing synaptic
70 abnormalities and consequently, cognitive deficits after brain irradiation. The underlying molecular
71 pathways responsible for the protective effects of repopulated microglia against radiotherapy-
72 induced neuronal alterations remain unknown.

73 In the current study, 1) we first defined signature of repopulating cells and analyzed the
74 transcriptional profile of repopulated brain macrophages from irradiated mouse brains after CSF-
75 1R inhibitor-mediated depletion. 2) We next sought to establish the origin of repopulated cells
76 coming from the peripheral monocytic lineage. 3) We identified the functionality of repopulated
77 macrophages by measuring the ability to engulf synaptic compartments compared to brain
78 resident microglia. Lastly, 4) we determined the protective properties of brain-engrafted
79 macrophages (BEMs) against a secondary concussive brain injury-induced cognitive deficits.
80 Together, these results uncover the mechanism by which brain-engrafted macrophages preserve
81 hippocampal synapses and memory functions after radiation injury and also in response to an
82 additional brain injury.

83

Results

Microglia depletion and repopulation prevents long term radiation-induced memory deficits and loss of hippocampal PSD95.

Temporary microglia depletion during or shortly after exposure to brain irradiation prevents cognitive deficits, suggesting microglia's key role in modifying neuronal and cognitive functions [12-14]. Changes in expression levels of pro-inflammatory cytokine/chemokines have been shown to correlate with cognitive performance in mice [12, 15, 20], however, the exact change in the transcriptional profile of repopulated microglia after brain irradiation is unknown and is an important tool to dissect the roles that repopulated microglia play in preventing of radiation-induced memory deficits. We performed RNA sequencing using repopulated microglia, FACS sorted from irradiated and control mouse brains after CSF-1Ri treatment, and compared with transcriptomes of microglia obtained from mice without CSF-1Ri treatment (**Figure 1a,b**). A CSF-1R inhibitor was used to fully deplete microglia in 8-weeks old male mice, for a duration of 21 days. Three fractions of therapeutic whole-brain irradiation were given to each mouse every other day over five days starting from day 7 of CSF-1R inhibitor treatment. Novel Object Recognition (NOR) test was used to measure recognition memory 4 weeks after the last fraction of WBRT. Consistent with our previous report, fractionated WBRT resulted in impairment in recognition memory, which was prevented by CSF-1R inhibitor treatment (**Figure 1a, lower panel**). One day after the NOR test, mice were euthanized and whole brains were used to sort microglia ($CD45^{low}CD11b^{+}$ population) for RNA extraction. We used samples from the five best performers in non-impaired groups (control diet + sham, CSF-1R inhibitor + sham/WBTR) and the five worst performers in the memory impaired group (control diet + WBRT) for RNA sequencing (**Figure 1a**).

We previously demonstrated that brain irradiation resulted in reduced density of dendritic spines in hippocampal neurons [13]. To accurately determine the effect of WBRT in the intrinsic synaptic protein levels we measured pre- and post-synaptic markers in the hippocampus by flow-

synaptometry [26, 27]. Fractionated hippocampal cell membranes containing synaptosomes were enriched and particles between 1 – 3 μm were analyzed to measure synaptic protein levels using mean fluorescent intensities by FACS (**Figure 1e**). We observed no changes in pre-synaptic Synapsin-1 protein levels in the hippocampi across all groups (**Figure 1f**). However, we measured a significant reduction in post-synaptic protein PSD-95 after WBRT, which was completely prevented by CSF-1R inhibitor mediated microglia depletion (**Figure 1g**). These results cement the role of microglia in the radiation-induced loss of post-synaptic components after WBRT.

Microglia depletion and repopulation eliminates radiation-induced transcriptome signatures

To identify biological pathways involved in radiation-induced memory deficits, we listed genes differentially expressed in microglia after WBRT with and without microglia depletion and repopulation for Gene Ontology Biological Process (GOBP) enrichment analysis. 204 genes were found to be differentially expressed (DE genes) only in microglia isolated from irradiated brains (**Figure 1b and Supplementary Table 1**). No enriched GOBP terms were found from the 87 WBRT down-regulated genes (Supplementary Table 1). There were 193 enriched GOBP terms from the 117 WBRT up-regulated genes, the top 20 enriched GOBP terms are listed in **Figure 1c.** Almost half (96) of these enriched GOBP terms were associated with increased response to cell cycle regulation, radiation, DNA repair and stress; the rest enriched GOBP terms were associated with increased metabolism (21), development (12), regulation of protein kinase activity (8), cellular adhesion (4) and other functions (**Figure 1d, Supplementary Table** 1). Notably, regardless of WBRT, the expression of these WBRT-induced DE genes did not change in cells isolated from brains treated with CSF-1Ri. These results demonstrate that the transcriptomic changes in microglia induced by WBRT can be completely eliminated after microglia depletion and repopulation.

133

134 *qPCR validation of the RNAseq results*

135 To validate the RNAseq results, we next performed qPCR analyses using sorted microglia from
136 animals in the same cohort (**Figure 1b,** and **Supplementary Table 1**). The expression of the toll-
137 like receptor 3 (TLR3) family gene *Lgals9* was significantly increased by irradiation (WBRT +
138 Control diet versus Sham + Control diet) and was at levels comparable to the shams (Sham +
139 Control diet) when treated with CSF-1Ri despite of irradiation (**Supplementary Figure S1a**).
140 *TNFα*, another TLR3 family member which also belongs to GOBP "regulation of response to
141 reactive oxygen species (ROS)", was significantly upregulated by irradiation (WBRT + Control
142 diet versus Sham + Control diet); its expression levels are comparable between the Sham +
143 Control diet and the WBRT + CSF1Ri treated groups. However, *TNFα* remained elevated in
144 microglia from mice treated only by CSF-1Ri (Supplementary Figure S1b). Another gene from the
145 GOBP "regulation of response to ROS", *Sesn2*, was also significantly upregulated by WBRT
146 (**Supplementary Figure S1c**). *Sesn2* remained at the control sham levels in CSF-1Ri only group
147 and was significantly down-regulated in the WBRT + CSF-1Ri group. *Mdm2*, a gene that belongs
148 to GOBP "cellular response to ionizing radiation", was increased after WBRT, and significantly
149 downregulated in in CSF-1Ri treated groups (Supplementary Figure S1d). Other WBRT-induced
150 expression of radiation induced genes, *Ddias*, *Rad51, FoxM1* and *Check 1*, were all at the control
151 sham levels in repopulated microglia regardless of the exposure to WBRT (**Supplementary**
152 **Figure S1 e – h**). In conclusion, the qPCR validation confirmed that the transcriptomic changes
153 seen in our RNAseq dataset were reliable. These results suggest that CSF-1Ri mediated
154 microglia depletion during WBRT followed by repopulation eliminated radiation-induced
155 signatures in the microglia transcriptome.

156

157 *Repopulated microglia after WBRT originate from peripheral monocytes*

158 The fractalkine receptor CX3CR1 is expressed in both microglia and peripheral monocytes [28],
159 while chemokine receptor CCR2 is mainly expressed in monocytes [29]. In the Cx3cr1$^{GFP/+}$Ccr2$^{RFP/+}$
160 reporter mice, the different expression patterns of GFP and RFP can be used to distinguish
161 microglia (GFP+RFP-) from monocytes (GFP+RFP+) [29]. To investigate the cell-of-origin of
162 repopulated microglia in our experimental paradigm we generated bone marrow chimeras with
163 head-protected irradiation using fluorescent labeled bone marrow from Cx3cr1$^{GFP/+}$Ccr2$^{RFP/+}$
164 donor mice (**Figure 2a**). This allowed partial replacement of bone marrow cells without changing
165 the permeability of the blood-brain-barrier [2, 30, 31]. At 6 weeks after bone marrow transplantation
166 about two thirds of peripheral monocytes were replaced by transplanted cells with fluorescent
167 labels (**Figure 2b**). Bone marrow chimera animals were then treated with WBRT and CSF-1R
168 inhibitor following the same experimental timeline used for RNA sequencing (**Figure 2a**). Next,
169 we compared the compositions of myeloid cells in the brain after CSF-1R inhibitor-mediated
170 depletion and repopulation. Flow cytometry analyses performed 33 days after WBRT revealed
171 that microglia depletion and repopulation alone (Sham + CSF-1Ri) only resulted in limited
172 accumulation of transplanted cells in the brain (**Figure 2c, BMT only**). However, in mice that
173 received WBRT and CSF-1Ri, two thirds of the microglia were replaced by Cx3cr1-GFP labeled
174 cells (**Figure 2c, BMT +fWBI**). These results suggest that microglia depletion during WBRT
175 resulted in significant contribution of the CNS microglia pool by peripheral monocyte-derived
176 BEMs.

177

178 *Brain-engrafted macrophages retain monocyte signatures*

179 We next assessed the transcriptomic signature of the BEMs after microglia depletion and WBRT
180 by comparing our RNAseq dataset with a previous report by Lavin and Winter *et al* [32]. To minimize

181 false discovery and noise signals, we examined 1201 genes from this published dataset with a
182 fold change greater than 1.50 or smaller than 0.667 for down-regulated genes ($p<0.05$, monocyte
183 compared to naïve microglia), and found that 1066 genes were expressed in our samples
184 (**Supplementary Table 2**). Strikingly, the hierarchical clustering of 525 monocyte- and 541
185 microglia-signature genes revealed that the expression profile of monocyte-derived BEMs (WBRT
186 + CSF-1Ri) does not cluster with naïve (Sham + Control diet), irradiated (WBRT + Control diet)
187 or repopulated (Sham + CSF-1Ri) microglia (**Figure 2d**). Similarity matrix analysis using this
188 microglia/monocyte signature gene list revealed that the expression pattern in BEMs is different
189 from naïve, irradiated and repopulated microglia (**Figure 2e**). Next, we counted genes in each
190 group that expressed in the same trends as microglia or monocyte signature genes from the Lavin
191 data set to determine the similarity scores to these two cell populations. We found that naïve,
192 irradiated and repopulated microglia had 60%, 57% and 51% (718, 685 and 612) genes
193 expressed in the same trends as microglia signature genes, respectively, with minimum similarity
194 (2-3%) to monocyte signature genes; while BEMs expressed both microglia (28%, 331 genes)
195 and monocyte signature genes (32%, 386 genes) (**Figure 2f**). These results further confirm that
196 after microglia depletion and WBRT BEMs originate from blood monocytes.

197

198 *qPCR validation of microglia- and monocyte-specific genes*

199 To validate microglia and monocyte signature genes that were differentially expressed in our
200 RNAseq results we next performed qPCR analyses (**Supplementary Figure 2 and**
201 **Supplementary Table 2**). Microglia signature genes *Sall1*, *P2ry12*, *Tmem119* and *Trem2* were
202 expressed at comparable levels in naïve, irradiated and repopulated microglia, while at
203 significantly lower level in BEMs (**Supplementary Figure 2 a – d**). On the other hand, expression
204 of monocyte signature gene *Runx3*, was significantly higher in BEMs than other groups
205 (**Supplementary Figure 2 e**). Notably, previously reported brain-engrafted macrophage specific

genes *Lpar6* and *Pmepa1* [33] have significantly higher expression levels in BEMs after CSF-1Ri and WBRT treatments compared to other groups (**Supplementary Figure 2 f and g**). In addition, the expression of *Ccr2*, a monocyte signature gene that was not differentially expressed in our RNAseq dataset, was also not differentially expressed among the four experimental groups by qPCR (**Supplementary Figure 2 h**). Taken together, these qPCR results validate our RNAseq results and cement the notion that BEMs after microglia depletion and WBRT originate from peripheral monocytes.

Monocyte-derived brain-engrafted macrophages resemble embryonic microglia signatures

Because monocyte-derived BEMs were exposed to the brain microenvironment for a short period of time, we hypothesized that they were functionally immature. To test this hypothesis, we first examined genes that were highly expressed at different developmental stages in microglia, and used yolk sac/embryonic and adult-specific genes as references (called embryonic and adult signature genes hereon) [34]. Hierarchical clustering of 1617 embryonic and 785 adult microglia signature genes revealed that transcriptomes of BEMs were highly similar to embryonic microglia, while the transcriptomes of microglia from other groups were similar to adult microglia and did not resemble the embryonic one (**Supplementary Figure S3a**). In addition, a similarity matrix analysis using all 2402 overlapped genes between two datasets showed that BEMs had the lowest similarity with microglia from other groups (**Supplementary Figure S3b**). In addition, 54% of the listed genes (n=1306) in BEMs expressed in the same trends as *yolk sac*/embryonic microglia compared to adult microglia (**Supplementary Figure S3c**). In contrast, naïve (Sham), irradiated (WBRT only) and repopulated microglia (CSF-1Ri only) had much lower embryonic signature similarity scores (16%, 19% and 17%, n=381, 445 and 405, respectively, Supplementary Figure S3c). Notably, naïve, irradiated and repopulated microglia transcriptomes had high adult signature similarity scores (69%, 59% and 63%, n=1649, 1409 and 1507,

231 respectively), while BEMs had the lowest adult similarity score (32%, n=759). These data suggest
232 that the monocyte-derived BEMs start to resemble microglia by expressing more embryonic than
233 adult microglia transcriptomic signature genes.

234

235 *Radiation-induced aberrant phagocytosis activity is abrogated in brain-engrafted macrophages*

236 Aberrant loss of synapses during neuroinflammatory conditions has been linked with increased
237 engulfment of synaptic compartments by microglia [35]. To determine if WBRT affects the
238 phagocytosis potency of microglia, we injected pre-labeled synaptosomes from a naïve donor
239 mouse into the hippocampi of mice after WBRT and CSF-1R inhibitor treatment and measured
240 engulfment by microglia using flow cytometry (**Figure 3a**). After WBRT there was a significant
241 increase in the number of microglia engulfing synaptosomes in the hippocampus compared to
242 naïve non-irradiated animals (**Figure 3b**). Strikingly, synapse engulfment activity was unchanged
243 compared to naïve animals in animals treated with CSF-1R inhibitor during WBRT (**Figure 3b**).
244 Immunofluorescent imaging at the injection sites confirmed that the injected synaptosomes were
245 indeed engulfed by microglia, and the increased trend of engulfment by irradiated microglia
246 remained unchanged (**Figures 3 c and d, Supplementary Figure 4a).** Notably, after
247 hippocampal injection of fluorescent labeled latex beads into the hippocampus, we found that
248 WBRT resulted in increased engulfment of latex beads was also inhibited by CSF-1R inhibitor
249 treatment, suggesting that the WBRT-induced increase of engulfment was not specific to
250 synaptosomes, but rather a general increase of phagocytosis potency (**Supplementary Figure**
251 **4b**). These data are the first to demonstrate that WBRT results in an increase in microglial
252 phagocytosis activity in the hippocampus that can be prevented by transient microglia depletion
253 and full repopulation.

254

255 *Irradiation-induced complement and phagocytic receptors expression in microglia are absent in*
256 *BEM after WBRT.*

257 Microglial complement receptors play essential roles in physiologic synaptic elimination during
258 development and aberrant elimination during neuroinflammatory conditions [35, 36]. To understand
259 the mechanisms of increased microglia phagocytic activity after WBRT, we measured expression
260 levels of a list of complement receptors, phagocytic markers and lysosome proteins in microglia
261 by flow cytometry. The expression of complement receptor C5aR was significantly elevated in
262 microglia at one month after WBRT. However, in animals treated with CSF-1Ri C5aR expression
263 was unchanged from naïve animals (**Figure 3e**). The same trend was observed in the expression
264 levels of CD68 and lysosomal-associated membrane protein 1 (LAMP-1) (**Figure 3 f and g**).
265 These results were consistent with our data demonstrating decreased PSD95 levels (Figure 3b)
266 and increased microglial phagocytosis activity in the hippocampus after WBRT (**Figure 3 b and**
267 **d**). In addition, complement receptor CR3 (CD11b) was significantly elevated in microglia after
268 WBRT or CSF-1Ri treatments alone, and remained unchanged in BEMs with combined WBRT
269 and CSF-1Ri treatments (**Supplementary Figure S5a**). No changes in the complement receptor
270 C3ar1 were measured after WBRT or CSF-1R inhibitor treatment (**Supplementary Figure S5b**).
271 These results demonstrate that the increased microglia phagocytosis of synaptosomes after
272 WBRT was associated with increased phagocytic and lysosome proteins, and was likely through
273 the complement pathways.

274

275 *Brain-engrafted macrophages after microglia depletion persist in the brain*

276 To determine whether BEMs are present long-term in the brain, we monitored this cellular
277 population for 6 months after WBRT. To eliminate the limitation of using bone marrow obtained
278 from the Cx3cr1$^{+/GFP}$Ccr2$^{+/RFP}$ knock-in reporter mouse strain, we used an actin-GFP transgenic

279 line as bone marrow donors and generated chimeras using the same body-only irradiation
280 protocol (**Figure 4 a**). Six weeks later, mice were treated with CSF-1R inhibitor and WBRT and
281 then used to trace BEMs at varies time points (**Figure 4 a**). Whole coronal sections at the level of
282 the dorsal hippocampus were stained with Iba1 and imaged to quantify total Iba1+ and GFP+
283 cells (**Supplementary Figure 6 a**). We found that all GFP+ cells in the brain were also Iba1+,
284 suggesting that BEMs were indeed derived from the periphery. In addition, the morphology of
285 Iba1+GFP+ BEMs were analyzed and compared to Iba1+GFP- microglia (**Figure 4 b and d**). We
286 found that round-shaped Iba1+GFP+ BEM cells entered the brain starting from 7 days after WBRT,
287 and started to obtain more processes that resembled microglia morphology (**Figure 4 b**). However,
288 Sholl analysis demonstrated that the morphology of BEMs remained stable from 33 days after
289 WBRT and never reached the structural complexity of microglia (**Figure 4c, Supplementary**
290 **Figure S7**). We found that 40 – 90% of Iba1+ cells are also GFP+ at 14 days after WBRT. This
291 ratio remained at high levels at 1, 3 and 6 months after WBRT (**Figure 4 e**). Interestingly, although
292 the Iba1+ and Iba1+GFP+ cell numbers are not fully recovered at 14 days after WBRT, the
293 microglia replacement ratio was similar to the level of later time points (Figure 5 e and
294 Supplementary Figure S6 b and c), suggesting a non-competitive manner of brain parenchyma
295 occupancy by microglia and BEMs. These data demonstrate that BEMs enter the brain shortly
296 after WBRT, adapt to a microglia-like morphology and maintain a stable population.

297

298 *BEMs provide long-term protection against WBRT-induced memory deficits and hippocampal*
299 *dendritic spine loss*

300 To measure the long-term cognitive outcomes, we treated a batch of wildtype animals, and tested
301 their recognition memory at 3 and 6 months after WBRT (**Figure 5 a**). We found that WBRT
302 resulted in persistent loss of recognition memory also at 3 and 6 months, while CSF-1Ri treatment
303 alone did not alter recognition memory performance (**Figure 5 b and c**). Strikingly, mice that

304 received WBRT along with temporary microglia depletion did not show any memory deficits and
305 performed undistinguishable from control animals at 3 and 6 months (**Figure 5 b and c**). Our
306 previous report demonstrated that WBRT-induced dendritic spine loss in hippocampal neurons
307 was fully prevented by temporary microglia depletion during irradiation (**Figure 5 d,** replotted
308 using previously published data) [13]. In this study, we sought to understand if the protective effects
309 persisted up to 6 months after WBRT. Our results clearly show that radiation-induced loss of
310 dendritic spines in hippocampal neurons persists to this time point, and that the protective effect
311 of microglia depletion and subsequent replacement by BEMs is long lasting (**Figure 5 e**). Taken
312 together, brief depletion of microglia during WBRT induces sustainable BEMs in the brain and
313 provides long-term protection against irradiation-induced deficits in recognition memory.

314

315 *Replacement of microglia by BEMs protects against concussive injury-induced memory loss*

316 To investigate the function of BEMs after they replaced microglia, a single mild concussive Closed
317 Head Injury (CHI) was given to mice 30 days after CSF-1R inhibitor treatment and WBRT;
318 microglia/BEMs morphology and phagocytic activities were measured following recognition
319 memory test by NOR (**Fig 6 a**). By FACS analysis at 24 days post injury, we found that
320 phagocytosis activity increased (p=0.0419) after CHI in microglia but not in BEMs (**Figure 6 b**).
321 Quantification of immunofluorescent staining of Iba-1/PSD-95 co-localization revealed a trend of
322 increased engulfment towards pre-stained synaptosomes by microglia but not by BEMs (**Fig 6 c**
323 **and d**). In addition, the structural complexity of microglia decreased in Sholl analysis, while the
324 morphology of BEMs remained unchanged after CHI (**Figure 6 e**). Furthermore, at 20 days after
325 injury, CHI-induced recognition memory deficits were spared in mice whose microglia were
326 replaced by BEMs (**Figure 6 f**). These results demonstrate that unlike resident microglia which
327 transition to a less ramified morphology and exhibit increased phagocytic activity towards injected
328 synaptosomes, BEMs remain unchanged in both morphology and phagocytic activity in response

329 to CHI. More importantly, our data suggest that replacement of microglia by BEMs can protect
330 against CHI-induced memory loss.

331

332

333 **Discussion**

334 Here we provide evidence for the direct involvement of microglia phagocytic activity
335 towards synaptic compartments as a mechanistic cause for loss of dendritic spines with
336 consequent impairments in memory functions after WBRT. Replacement of microglia with
337 monocyte derived BEMs prevents loss of synapses and consequent memory deficits. Importantly,
338 BEMs replacing microglia are also protective against a second injury to the brain. Together our
339 results unravel novel immediate and long lasting therapeutic benefits of microglia depletion and
340 repopulation during WBRT.

341 Microglia play pivotal roles in reshaping synaptic networks during neonatal brain
342 development [37, 38]. They engulf synaptic elements by active synaptic pruning in an activity- and
343 complement-dependent manner [38]. Microglia-driven aberrant loss of synapses and consequent
344 impairment of cognitive functions have also been reported in animal models of AD [35], infection [39],
345 injury [40, 41], and aging [42]. Using RNA sequencing, we compared the transcriptomes of microglia
346 from irradiated and non-irradiated brains after CSF-1Ri-mediated microglia depletion and
347 repopulation. WBRT induces increased expression of genes that mainly belong to cell cycle
348 regulation, DNA damage repair and stress-induced biological processes (**Figure 1d**). As a result,
349 activated microglia have higher engulfing potential towards both intrinsic and extrinsic synaptic
350 compartments (**Figures 1 g, Figure 3 b - d**). This view is further supported by the increased
351 expression of endosome/lysosome proteins CD68 and CD107a with the complement receptors
352 CR3 and C5ar1 measured in microglia chronically after WBRT (**Figure 3 e – g, and**
353 **Supplementary Figure 5**). Notably, both endosome/lysosome proteins and complement receptor

354 expressions were comparable to naïve microglia (sham + control diet) in BEMs (WBRT + CSF-
355 1Ri) and repopulated microglia (CSF-1Ri only). These results suggest that the loss of
356 hippocampal synapses after WBRT may be dependent on the activation of the alternative
357 complement pathway. Interestingly, although BEMs are morphologically similar to adult microglia,
358 they retain a transcriptomic signature similar to both circulating monocytes and embryonic
359 microglia (**Figure 2 and Supplementary Figure 3**). It is plausible that the BEMs are in a
360 transitional state between peripheral monocytes and CNS microglia at early developmental
361 stages.

362 The decrease in post-synaptic protein PSD95 level in hippocampal synaptosomes is also
363 paralleled with reductions in hippocampal dendritic spines (**Figures 5 d, e and Feng et al**[13]).
364 However, pre-synaptic Synapsin 1 protein levels are not affected by WBRT or microglia depletion,
365 suggesting that WBRT mainly induces loss of post-synaptic compartments. Interestingly, although
366 the phagocytosis potency of repopulated microglia and BEMs are both low (**Figures 3 b and d**),
367 microglia depletion and repopulation alone does not affect dendritic spine density (**Figures 5 d**
368 **and e**). On the other hand, microglia replacement by BEMs results in increased dendritic spine
369 density compared to those with radiation alone, and microglia depletion alone (**Figure 5 d, data**
370 **re-plotted from Feng et al**[13]). Strikingly, the protective effect of microglia depletion during WBRT
371 results in intact memory functions and extends to 3- and 6-months following irradiation (**Figure 5**
372 **b and c**). The dendritic spine density in mice that received WBRT and CSF-1Ri remained higher
373 than those who only received CSF-1Ri (**Figure 5 e**) suggesting that in an non-reactivate state
374 (evidenced by no changes in genes involved in cell cycle and radiation response, in microglial
375 phagocytosis and lysosome proteins, or in phagocytosis activity towards injected synaptosomes
376 and latex beads) of repopulated microglia and BEMs may have intrinsic differences in maintaining
377 the homeostasis of dendritic spines, which appears to diminish over time.

In the CNS, microglia maintain a stable population by self-renewal in either a random manner or through clonal expansion [3, 43]. CSF-1R inhibitor treatment alone results in acute depletion of up to 99% of CNS resident microglia, with repopulated microglia arising solely from the residual microglia and their progenitor cells that remain after treatment [8, 44]. The repopulated microglia have transcriptional and functional profiles similar to naïve microglia [9]. Peripheral macrophages can engraft into the brain but remain morphologically, transcriptionally and functionally different from CNS resident microglia [45, 46,]. Under specific circumstances, monocytes entering the CNS can become microglia-like cells. This is most clearly demonstrated in experiments where lethal whole-body irradiation was followed by bone marrow transplantation with labeled monocytes ($Ccr2^{+}Ly6C^{high}$), resulting in accumulation of these cells in the brain [30]. In neonatal mouse brains monocytes can enter the brain parenchyma without head irradiation and become microglia-like cells at a low frequency [47]. In addition, chronic depletion of microglia without irradiation also results in myeloid cells entering the CNS and becoming BEMs [33]. However, the roles of BEMs in cognitive functions are largely unknown. Here we report that concurrent microglia depletion and therapeutic brain irradiation causes peripheral monocytes to enter the brain parenchyma and become microglia-like BEMs. BEMs enter the brain at 14 days after the completion of brain irradiation, or 4 days after the CSF-1Ri withdrawal (**Figure 4 e, and Supplementary Figure 6**). Notably, although the ratio of BEMs was high at this time point the total number of Iba1 positive cells is not fully recovered (**Supplementary Figure 6 b**). This ratio remains at high levels in head-irradiated mice throughout the current study (**Figure 5 e**), suggesting that microglia depletion during WBRT results in sustainable replacement of microglia by BEMs. Importantly, this observation correlates with long-term protection against WBRT-induced loss of recognition memory and dendritic spines in hippocampal granule neurons (**Figure 6 b – e**).

402 In the clinic, cancer patients are unlikely to receive a second round of radiotherapy to the
403 brain. Therefore, instead of introducing a second round of WBRT, after they occupied the brain
404 we gave BEM-bearing mice CHI that causes memory deficits[48, 49], and further examined BEMs'
405 response to a single head trauma. Our data show that microglia had increased phagocytic
406 potential to injected synaptosomes after CHI, while phagocytic activity of BEMs did not change
407 and remained at a similar level as naïve microglia (**Figure 6 b and c**). This is further demonstrated
408 by Sholl analysis of BEMs showing no change in morphology after CHI (**Figure 6 e**). Most
409 importantly, CHI-induced memory deficit was prevented in BEM-bearing mice (**Figure 7 f**). These
410 data are the first to demonstrate that BEMs can prevent brain injury-induced cognitive dysfunction.

411 Further lineage tracing, transcriptomic and functional studies with different microglia
412 depletion models will help answer the following questions: 1) whether the delayed engraftment of
413 BEMs after WBRT seen at day 14 is due to the suppression of cell trafficking from the periphery
414 to the CNS or survival of newly engrafted BEMs that depend on the CSF-1R. 2) The mechanism
415 of the long-term maintenance of BEMs after WBRT. Whether it is achieved by continuous
416 engraftment of new BEMs or by colonization of BEMs that are already in the brain parenchyma.

417 In conclusion we report evidence for the mechanism by which microglia depletion and
418 repopulation after WRBT prevents memory loss. Our results demonstrate that replacement of
419 CNS resident microglia by peripheral monocyte-derived BEMs results in a transcriptional and
420 functional reset of immune cells in the brain to an inactive state, which spares the brain from
421 WBRT-induced dendritic spine loss in hippocampal neurons and recognition memory deficits.
422 Most importantly, replacement of microglia by BEMs protects against concussive brain injury-
423 induced cognitive deficits. These results suggest that replacement of depleted microglia pool by
424 peripheral monocyte-derived BEMs represents a potent treatment for irradiation-induced memory
425 deficits.

426

427

428 **Materials and Methods**

429 **Animals:** All experiments were conducted in compliance with protocols approved by the
430 Institutional Animal Care and Use Committee at the University of California, San Francisco
431 (UCSF), following the National Institutes of Health Guidelines for Animal Care. 7 weeks old
432 C57BL/6J male mice were purchased from the Jackson Laboratory and housed at UCSF animal
433 facilities and were provided with food and water ad libitum. All mice were habituated for one week
434 before any treatments or procedures. 8–10 weeks old Cx3cr1$^{GFP/+}$Ccr2$^{RFP/+}$ mice were breed by
435 crossing the Cx3cr1$^{GFP/GFP}$Ccr2$^{RFP/RFP}$ line with wildtype C57BL/6J mice, and used as donors for
436 the bone marrow chimeras.

437 **CSF-1Ri treatment:** CSF-1Ri (PLX5622 formulated in AIN-76A standard chow at 1200 ppm,
438 Research Diets, Inc) were provided by Plexxikon, Inc (Berkeley, CA). Mice were given free access
439 to either CSF-1Ri chow or control diet (AIN-76A without PLX5622) for 21 days. Approximately 4.8
440 mg of PLX5622 was ingested by each mouse per day in the treated group (calculation based on
441 4 g/mouse daily consumption).

442 **Fractionated whole-brain radiotherapy (WBRT):** 8 weeks old mice were injected with ketamine
443 (90mg/kg) /Xylazine (10 mg/kg) mix. When fully immobilized mice were placed in irradiator with
444 cesium-137 source at the dose rate of 2.58 Gy/min. The body was shielded with a lead collimator
445 that limited the radiation beam to a width of 1 cm to cover the brain. Three radiation fractions (3.3
446 Gy) were delivered every other day over 5 days. Sham animals received ketamine/xylazine
447 without irradiation.

448 **Bone marrow chimeras:** 8 weeks old C57BL/6J mice were used as bone marrow recipients. 8
449 weeks old males received two doses of 6 Gy cersium-137 irradiation at the dose rate of 2.58
450 Gy/min with head protected by lead plates 6 hours apart. Bone marrow cells from 6–10 weeks old
451 donors Cx3cr1$^{+/GFP}$Ccr2$^{+/RFP}$ or B6-EGFP (The Jackson Laboratory, stock No 003291) were
452 isolated and resuspended in sterile saline at a concentration of 100 million cells/ml. 0.1 ml of bone

453 marrow cells were injected into recipients via retro-orbital injection immediately after the second
454 head protected irradiation. Bone marrow chimeras were housed with 1.1 mg/ml neomycin as
455 drinking water for 4 weeks and allowed an additional 2 weeks to recover before any treatments.

456 **Concussive TBI – Closed head injury:** 12 weeks old C57BL/6J mice were randomly assigned
457 to each TBI or sham surgery group. Animals were anesthetized and maintained at 2-2.5%
458 isoflurane during CHI or sham surgery. Animals were secured to a stereotaxic frame with
459 nontraumatic ear bars and the head of the animal was supported with foam. Contusion was
460 induced using a 5-mm tip attached to an electromagnetic impactor (Leica) at the following
461 coordinates: anteroposterior, −1.50 mm and mediolateral, 0 mm with respect to bregma. The
462 contusion was produced with an impact depth of 1 mm from the surface of the skull with a velocity
463 of 5.0 m/s sustained for 300 ms. Animals that had a fractured skull after injury were excluded from
464 the study. Sham animals were secured to a stereotaxic frame with nontraumatic ear bars and
465 received the midline skin incision but no impact. After CHI or sham surgery, the scalp was sutured
466 and the animal was allowed to recover in an incubation chamber set to 37 °C. All animals
467 recovered from the surgical procedures as exhibited by normal behavior and weight maintenance
468 monitored throughout the duration of the experiments.

469 **Synaptosome isolation staining and injection:** Fresh hippocampi from a naïve mouse was
470 homogenized and spun down in 0.32M sucrose solution (dissolved in 50 mM HEPES buffer).
471 Supernatant was centrifuged in 0.65M sucrose solution at 12,000 rpm for 30 minutes at 4°C. The
472 synaptosome containing pellet was resuspended in 1 x ice-cold PBS, diluted to 100 µg/ml, and
473 stained with PSD-95 antibody (Millipore) on ice for 30 minutes followed by a secondary antibody
474 staining (Invitrogen, goat anti-mouse AF488). Stained synaptosomes were washed and diluted
475 20 times in PBS and stored at -80°C. 2 µl of pre-stained synaptosomes were injected into the
476 right hippocampus of each recipient mouse at the coordinate relative to the bregma: AP + 1.6 mm,
477 ML + 1.6 mm and DV -2.0 mm. Mice were euthanized 3 days later. The left hemispheres

478 (uninjected) were used for phagocytosis markers staining and the right hemispheres (injected)
479 were used to assess synaptosome phagocytosis levels by flow cytometry or immunofluorescent
480 staining.

481 **Immunofluorescent Staining:** hemi-brains with synaptosome injection were fixed in 4% PFA
482 overnight, cryo-protected in 30% sucrose solution in 1 x PBS and sliced in 20 μm sections. Sliced
483 tissues were stained with Iba1 (Fujifilm Wako Pure Chemical Corporation, 019-19741) followed
484 by a secondary antibody staining (goat anti-rabbit AF568, Invitrogen, A-11011). DAPI was used
485 for nuclear staining. Images close to the injection site (Supplementary Figure 1a) were taken using
486 a Zeiss Imager Z1 microscope under a 20x objective lens. Tissues from bone marrow chimeras
487 were processed and stained as described above. Images were taken using a CSU-W1 Nikon
488 Spinning Disk Confocal microscope under 10x air, 20x air or 100x immerse oil lenses. All images
489 were analyzed using the Fiji/ImageJ software by experimenters blinded to sample information.

490 **Behavior test:** Novel Object Recognition (NOR) task was used to test hippocampal dependent
491 recognition memory at one, three and six months after the last dose of irradiation. All tests took
492 place during the dark cycle in a room with dim red light as previously described [13, 14]. Briefly, mice
493 were habituated in an open arena (30 cm x 30 cm x 30 cm, L x W x H) for 10 minutes on day one
494 and day two. On day three, two identical objects were put into the arena at a distance of 21 cm
495 and mice were allowed to explore for 5 minutes. On day four, one object was replaced by a novel
496 object and mice were allowed to explore for 5 minutes. All trials were recorded by an overhead
497 camera and analyzed using Ethovision software. Data are presented as discrimination Index,
498 calculated using fomular $DI = (T_{Novel} - T_{Familiar})/(T_{Novel} + T_{Familiar})$.

499 **Flow cytometry:** mice were perfused with cold PBS after euthanasia. Brains were immediately
500 removed and dissociated using a Neural Tissue Dissociation kit (P) (Miltenyi Biotec). Brain cells
501 were resuspended in 30% Percoll solution diluted in RPMI medium, and centrifuged at 800 g for
502 30 minutes at 4°C. Cell pellets were washed with FACS buffer (1 x DPBS with 0.5% BSA fraction

503 V and 2% FBS), blocked with mouse CD16/32 Fc block (BD Biosciences #553141) and stained
504 with fluorophore conjugated antibodies (CD11b-AF700, CD45-FITC, BD Pharmingen 557690 and
505 553080, C5aR-PE, CD68-PE and CD107a-PE, Miltenyi Biotec 130-106-174, 130-102-923 and
506 130-102-219), washed with FACS buffer and used for sort or analyses of bone marrow chimera
507 efficiency. Data were collected on an Aria III sorter using the FACSDIVA software (BD
508 Biosciences, V8.0.1), and analyzed with Flowjo software (FlowJo, LLC, V10.4.2).

509 **Flow synaptometry**: after isolation (described above) synaptosomes were stained with PSD-95
510 (Abcam ab13552) or Synapsin-1 (Millipore #1543) antibodies on ice for 30 minutes, washed and
511 followed by a secondary antibody staining (Invitrogen, goat anti-mouse AF488, A-11001). Stained
512 synaptosomes were used immediately for analysis of mean fluorescent intensity measurement.
513 Fluorescent latex beads of 1 μm, 2 μm, 3 μm and 6 μm were used as references of particle sizes
514 in the FSC-A vs SSC-A dot plot. Events between 1 μm and 3 μm were used to measure mean
515 fluorescent intensities of isolated synaptosomes under the FITC channel. Data were collected on
516 an Aria III sorter using the FACSDIVA software, and analyzed with Flowjo software. At least
517 100,000 events were collected from each sample for the analyses.

518 **RNA sequencing:** mRNA was isolated from 100,000 to 400,000 sorted microglia or BEMs using
519 the Dynabeads mRNA DIRECT Purification Kit (Invitrogen #61011) following the manufacturer's
520 instructions. RNA sequencing libraries were generated using the Ovation RNA-seq system V2
521 and Ultralow Library Construction System sample prep kits (NuGEN). Libraries were sequenced
522 on the HiSeq 2500 to generate single end 50bp reads according to the manufacturer's instructions.
523 Normalized per-gene read counts were used to compare relative gene expression levels across
524 samples. Only genes with average read counts greater than 10 were included for analyses.
525 Heatmaps were drawn using the online analysis software Morpheus (Broad Institute,
526 https://software.broadinstitute.org/morpheus), followed by hierarchical clustering using the One
527 minus pearson correlation method. Gene Ontology analysis was performed using the Statistical

528 overrepresentation test (GO biological process complete, PANTHER version 14) [50]. Bar graphs
529 to visualize fold enrichment and p values of enriched GO biological pathways were drawn using
530 the GraphPad Prism software (V 7.01, GraphPad Software, Inc). For analysis of
531 monocyte/microglia signature genes, dataset from Lavin and Winter et al was used as reference
532 (GSE63340) [32]. Genes significantly up or down regulated ($p<0.05$, fold-change > 1.5 or <0.667)
533 in monocytes vs microglia comparisons are defined as monocyte or microglia signature genes,
534 respectively. Heatmaps were drawn as described above, and similarity matrix were drawn using
535 the Morpheus online tool with Pearson correlation. Monocyte/microglia similarity scores were
536 calculated based on the numbers of genes in each treatment group from this study that expressed
537 in the same trend as monocyte/microglia signature genes (genes with fold-change between
538 0.6667 and 1.500 or with $p>0.05$ were defined as unspecified). For juvenile/embryonic signature
539 analysis, dataset from Matcovitch-Natan and Winter et al was used as reference (GSE79819) [34].
540 Gene listed to be highly expressed in Yolk Sac and embryonic day 10.5–12.5 were defined as
541 embryonic/juvenile microglia signatures, genes highly expressed in adult
542 cortex/hippocampus/spinal cord were defined as adult microglia signatures. Heatmaps, similarity
543 matrix and similarity scores were drawn or calculated as described above.

544 **qPCR:** mRNAs were extracted from sorted microglia using the Dynabeads mRNA DIRECT
545 Purification Kit (Invitrogen #61011), and reverse transcribed into cDNAs using reverse
546 transcription kit (info) . qPCR reactions were set up in duplicate reactions using the PowerUp
547 SYBR Green Master Mix kit (Applied Biosystems #A25777) using an Mx3000P qPCR System
548 (Agilent, Santa Clara, CA) following the manufacturer's instructions. Data were analyzed using
549 the standard curve method. Standard cDNAs were generated with total RNAs from mixed naïve
550 and irradiated mouse brains. qPCR primers sequences are listed in Supplementary Table 4.

551 **Sholl analysis:** Images of GFP+ (BEMs from bone marrow chimeras) or Iba1+ (AF555, all
552 microglia cells, and BEMs from non-bone marrow chimeras) cells were acquired from stained

553 frozen sections (20um) using a confocal microscope under 100x objectives (CSU-W1 Spinning
554 Disk/High Speed Widefield, Nikon). Max Z-projections from Z-stack images (0.26um step size)
555 were used for Sholl analysis[51] in Fiji[52] software using the following settings: manually defined cell
556 center at the cell body, the numbers of intersections between cellular processes and circles with
557 incremental radius (2um step size, up to 60um) were recorded, plotted and compared across
558 samples.

559 **Statistical analyses:** Two-way ANOVA was used to determine radiation and CSF-1Ri treatment
560 effects for NOR, qPCR, flowsynaptometry, flow cytometry, immunofluorescent staining counts
561 and dendritic spine count results, with Tukey's post hoc multiple comparisons. One-way ANOVA
562 with Sidak's post hoc multiple comparisons was used to determine effect of developmental stages
563 for dataset published by Matcovitch-Natan and Winter et al. Unpaired t-test was used to determine
564 differentially expressed microglia/monocyte signature genes from dataset published by Lavin and
565 Winter et al. Unpaired t-test was used calculate the p value of the comparison of BEMs
566 contributions between the BMT and BMT + WBRT groups. Exact p values and numbers of animals
567 used in each experiment were listed in each related figure legend. All error bars represent mean
568 ± SEM.

569

570 **Reference**

571 1. Alliot, F., Godin, I. & Pessac, B. Microglia derive from progenitors, originating from the yolk sac,
572 and which proliferate in the brain. *Developmental Brain Research* **117**, 145-152 (1999).
573 2. Ginhoux, F. *et al.* Fate Mapping Analysis Reveals That Adult Microglia Derive from Primitive
574 Macrophages. *Science* **330**, 841 (2010).
575 3. Ajami, B., Bennett, J.L., Krieger, C., Tetzlaff, W. & Rossi, F.M.V. Local self-renewal can sustain
576 CNS microglia maintenance and function throughout adult life. *Nature Neuroscience* **10**, 1538
577 (2007).
578 4. Prinz, M., Priller, J., Sisodia, S.S. & Ransohoff, R.M. Heterogeneity of CNS myeloid cells and their
579 roles in neurodegeneration. *Nat Neurosci* **14**, 1227-1235 (2011).
580 5. Saijo, K. & Glass, C.K. Microglial cell origin and phenotypes in health and disease. *Nat Rev*
581 *Immunol* **11**, 775-787 (2011).

582 6. Hong, S., Dissing-Olesen, L. & Stevens, B. New insights on the role of microglia in synaptic
583 pruning in health and disease. *Current opinion in neurobiology* **36**, 128-134 (2015).
584 7. Hong, S. & Stevens, B. Microglia: Phagocytosing to Clear, Sculpt, and Eliminate. *Developmental*
585 *Cell* **38**, 126-128 (2016).
586 8. Elmore, M.R. *et al.* Colony-stimulating factor 1 receptor signaling is necessary for microglia
587 viability, unmasking a microglia progenitor cell in the adult brain. *Neuron* **82**, 380-397 (2014).
588 9. Elmore, M.R., Lee, R.J., West, B.L. & Green, K.N. Characterizing newly repopulated microglia in
589 the adult mouse: impacts on animal behavior, cell morphology, and neuroinflammation. *PLoS*
590 *One* **10**, e0122912 (2015).
591 10. Dagher, N.N. *et al.* Colony-stimulating factor 1 receptor inhibition prevents microglial plaque
592 association and improves cognition in 3xTg-AD mice. *Journal of neuroinflammation* **12**, 139
593 (2015).
594 11. Spangenberg, E.E. *et al.* Eliminating microglia in Alzheimer's mice prevents neuronal loss without
595 modulating amyloid-β pathology. *Brain* (2016).
596 12. Acharya, M.M. *et al.* Elimination of microglia improves cognitive function following cranial
597 irradiation. *Scientific reports* **6**, 31545 (2016).
598 13. Feng, X. *et al.* Colony-stimulating factor 1 receptor blockade prevents fractionated whole-brain
599 irradiation-induced memory deficits. *Journal of neuroinflammation* **13**, 215 (2016).
600 14. Feng, X., Liu, S., Chen, D., Rosi, S. & Gupta, N. Rescue of cognitive function following fractionated
601 brain irradiation in a novel preclinical glioma model. *eLife* **7**, e38865 (2018).
602 15. Krukowski, K. *et al.* Temporary microglia-depletion after cosmic radiation modifies phagocytic
603 activity and prevents cognitive deficits. *Scientific reports* **8**, 7857 (2018).
604 16. Rapp, S.R. *et al.* Donepezil for Irradiated Brain Tumor Survivors: A Phase III Randomized Placebo-
605 Controlled Clinical Trial. *Journal of Clinical Oncology* **33**, 1653-1659 (2015).
606 17. Stupp, R. *et al.* Radiotherapy plus Concomitant and Adjuvant Temozolomide for Glioblastoma.
607 *New England Journal of Medicine* **352**, 987-996 (2005).
608 18. Greene-Schloesser, D. & Robbins, M.E. Radiation-induced cognitive impairment--from bench to
609 bedside. *Neuro Oncol* **14 Suppl 4**, iv37-44 (2012).
610 19. Shinohara, C., Gobbel, G.T., Lamborn, K.R., Tada, E. & Fike, J.R. Apoptosis in the Subependyma of
611 Young Adult Rats after Single and Fractionated Doses of X-Rays. *Cancer Research* **57**, 2694-2702
612 (1997).
613 20. Morganti, J.M., Jopson, T.D., Liu, S., Gupta, N. & Rosi, S. Cranial Irradiation Alters the Brain's
614 Microenvironment and Permits $CCR2^+$ Macrophage Infiltration. *PLoS ONE* **9**, e93650 (2014).
615 21. Warrington, J.P. *et al.* Whole Brain Radiation-Induced Vascular Cognitive Impairment:
616 Mechanisms and Implications. *Journal of Vascular Research* **50**, 445-457 (2013).
617 22. Hua, K., Schindler, M.K., McQuail, J.A., Forbes, M.E. & Riddle, D.R. Regionally distinct responses
618 of microglia and glial progenitor cells to whole brain irradiation in adult and aging rats. *PLoS One*
619 **7**, e52728 (2012).
620 23. Chiang, C.S., McBride, W.H. & Withers, H.R. Radiation-induced astrocytic and microglial
621 responses in mouse brain. *Radiotherapy and Oncology* **29**, 60-68 (1993).
622 24. Mizumatsu, S. *et al.* Extreme Sensitivity of Adult Neurogenesis to Low Doses of X-Irradiation.
623 *Cancer Research* **63**, 4021-4027 (2003).
624 25. Monje, M.L. *et al.* Impaired human hippocampal neurogenesis after treatment for central
625 nervous system malignancies. *Annals of Neurology* **62**, 515-520 (2007).
626 26. Fein, J.A. *et al.* Co-localization of amyloid beta and tau pathology in Alzheimer's disease
627 synaptosomes. *The American journal of pathology* **172**, 1683-1692 (2008).

27. Prieto, G.A. *et al.* Synapse-specific IL-1 receptor subunit reconfiguration augments vulnerability to IL-1β in the aged hippocampus. *Proceedings of the National Academy of Sciences* **112**, E5078 (2015).
28. Jung, S. *et al.* Analysis of Fractalkine Receptor CX₃CR1 Function by Targeted Deletion and Green Fluorescent Protein Reporter Gene Insertion. *Molecular and cellular biology* **20**, 4106 (2000).
29. Saederup, N. *et al.* Selective Chemokine Receptor Usage by Central Nervous System Myeloid Cells in CCR2-Red Fluorescent Protein Knock-In Mice. *PLoS ONE* **5**, e13693 (2010).
30. Mildner, A. *et al.* Microglia in the adult brain arise from Ly-6ChiCCR2+ monocytes only under defined host conditions. *Nat Neurosci* **10**, 1544-1553 (2007).
31. Priller, J. *et al.* Targeting gene-modified hematopoietic cells to the central nervous system: Use of green fluorescent protein uncovers microglial engraftment. *Nature Medicine* **7**, 1356-1361 (2001).
32. Lavin, Y. *et al.* Tissue-resident macrophage enhancer landscapes are shaped by the local microenvironment. *Cell* **159**, 1312-1326 (2014).
33. Cronk, J.C. *et al.* Peripherally derived macrophages can engraft the brain independent of irradiation and maintain an identity distinct from microglia. *The Journal of experimental medicine* **215**, 1627-1647 (2018).
34. Matcovitch-Natan, O. *et al.* Microglia development follows a stepwise program to regulate brain homeostasis. *Science* **353**, aad8670 (2016).
35. Hong, S. *et al.* Complement and microglia mediate early synapse loss in Alzheimer mouse models. *Science* (2016).
36. Stevens, B. *et al.* The classical complement cascade mediates CNS synapse elimination. *Cell* **131**, 1164-1178 (2007).
37. Vainchtein, I.D. *et al.* Astrocyte-derived interleukin-33 promotes microglial synapse engulfment and neural circuit development. *Science* **359**, 1269 (2018).
38. Schafer, Dorothy P. *et al.* Microglia Sculpt Postnatal Neural Circuits in an Activity and Complement-Dependent Manner. *Neuron* **74**, 691-705 (2012).
39. Vasek, M.J. *et al.* A complement-microglial axis drives synapse loss during virus-induced memory impairment. *Nature* **534**, 538-543 (2016).
40. Norris, G.T. *et al.* Neuronal integrity and complement control synaptic material clearance by microglia after CNS injury. *The Journal of experimental medicine* (2018).
41. Krukowski, K. *et al.* Traumatic Brain Injury in Aged Mice Induces Chronic Microglia Activation, Synapse Loss, and Complement-Dependent Memory Deficits. *International Journal of Molecular Sciences* **19** (2018).
42. Shi, Q. *et al.* Complement C3-Deficient Mice Fail to Display Age-Related Hippocampal Decline. *The Journal of neuroscience : the official journal of the Society for Neuroscience* **35**, 13029-13042 (2015).
43. Tay, T.L. *et al.* A new fate mapping system reveals context-dependent random or clonal expansion of microglia. *Nature Neuroscience* **20**, 793 (2017).
44. Huang, Y. *et al.* Repopulated microglia are solely derived from the proliferation of residual microglia after acute depletion. *Nat Neurosci* **21**, 530-540 (2018).
45. Ajami, B., Bennett, J.L., Krieger, C., McNagny, K.M. & Rossi, F.M.V. Infiltrating monocytes trigger EAE progression, but do not contribute to the resident microglia pool. *Nat Neurosci* **14**, 1142-1149 (2011).
46. Yamasaki, R. *et al.* Differential roles of microglia and monocytes in the inflamed central nervous system. *The Journal of experimental medicine* **211**, 1533-1549 (2014).

675 47. Chen, H.-R. *et al.* Fate mapping via CCR2-CreER mice reveals monocyte-to-microglia transition in
676 development and neonatal stroke. *Science Advances* **6**, eabb2119 (2020).
677 48. Chou, A. *et al.* Inhibition of the integrated stress response reverses cognitive deficits after
678 traumatic brain injury. *Proceedings of the National Academy of Sciences* **114**, E6420 (2017).
679 49. Krukowski, K. *et al.* Integrated Stress Response Inhibitor Reverses Sex-Dependent Behavioral and
680 Cell-Specific Deficits after Mild Repetitive Head Trauma. *Journal of Neurotrauma* **37**, 1370-1380
681 (2019).
682 50. Mi, H., Muruganujan, A., Ebert, D., Huang, X. & Thomas, P.D. PANTHER version 14: more
683 genomes, a new PANTHER GO-slim and improvements in enrichment analysis tools. *Nucleic*
684 *acids research* **47**, D419-D426 (2019).
685 51. Ferreira, T.A. & Blackman, A.V. Neuronal morphometry directly from bitmap images. **11**, 982-
686 984 (2014).
687 52. Schindelin, J. *et al.* Fiji: an open-source platform for biological-image analysis. *Nature methods* **9**,
688 676-682 (2012).
689 53. Feng, X. *et al.* Loss of CX3CR1 increases accumulation of inflammatory monocytes and promotes
690 gliomagenesis. *Oncotarget; Vol 6, No 17* (2015).

691

692

Acknowledgements

We thank the Nikon Imaging Center at UCSF for assistance with confocal microscope. We thank the Laboratory for Cell Analysis at UCSF for assistance with FACS sort and analysis.

Funding: This work was funded by grants from the National Institutes of Health no. R01CA133216, R01CA213441 and R01AG056770 (S.R.).

Author contributions

X.F. conceptualized the study, designed and performed the experiments, analyzed the data and wrote the manuscript. E.F. performed experiments, analyzed the data and wrote the manuscript. M.P performed experiments, analyzed the data and revised the manuscript. D.C. assisted in the in vivo phagocytosis assay and data analysis. Z.B. helped with the in vivo phagocytosis assay imaging and data analysis. M.B. assisted in the Sholl analysis of microglia and BEMs. S.G analyzed the long-term dendritic spine counts data. S.L. provided assistance in experiments related to WBRT and BM chimeras. N.G. provided critical inputs to the study and revised the manuscript. S.R. conceptualized and supervised the study and revised the manuscript. All authors approved the final version of the manuscript.

Competing interests

The authors declare no competing interests.

Figures

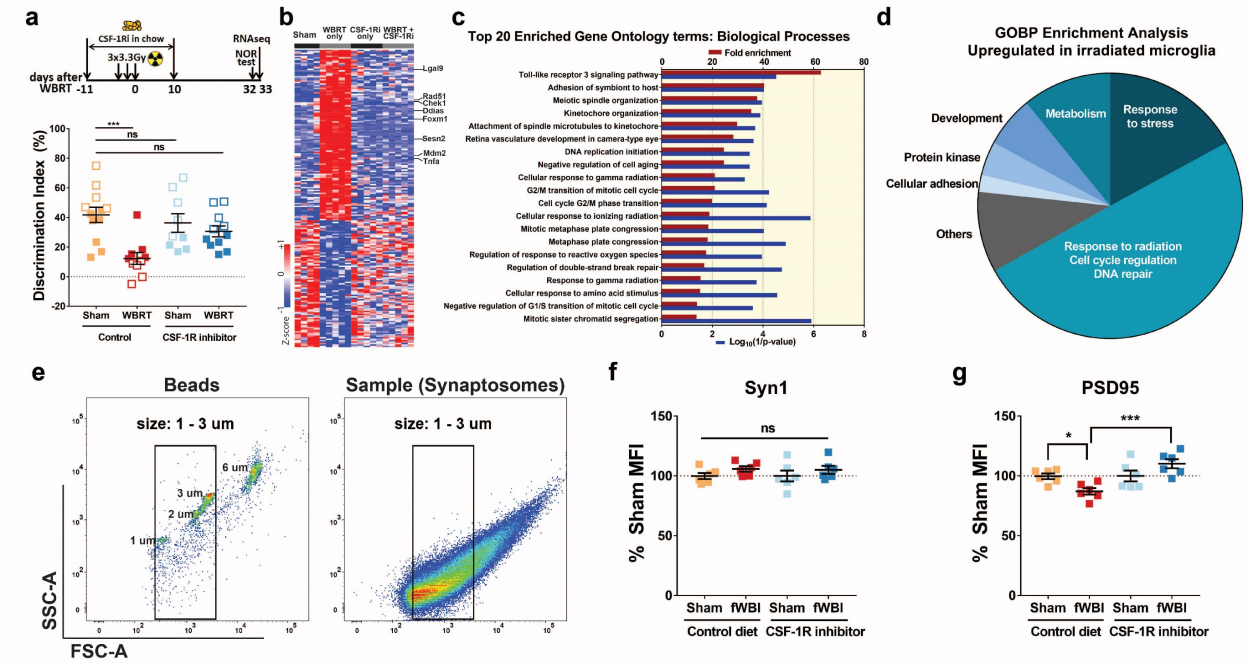

Figure 1: Microglia depletion and repopulation prevents long term radiation-induced memory deficits and loss of hippocampal PSD95. a experimental design and Novel Object Recognition (NOR) test result. CSF-1R inhibitor was used to deplete microglia during 3 doses of 3.3 Gy of whole-brain radiotherapy (WBRT). A 4-day NOR protocol was used to measure recognition memory, which ended on day 32 post WBRT. Microglia were isolated using fluorescent activated cell sorting (FACS) on day 33. and dot plots showing NOR results. Statistical analysis was performed using two-way ANOVA with Dunnett's multiple comparisons test. There is no CSF-1Ri treatment effect ($F(1,38)=1.787$, $p=0.1893$), but significant WBRT effect ($F(1, 38)=13.23$, $p=0.0008$) and interaction between CSF-1Ri treatment and WBRT ($F(1,38)=6.07$, $p=0.0184$), N = 9-12, animals with insufficient exploration time on NOR test day were excluded. Hollow squares represent animals used in RNA sequencing. **b** hierarchically clustered heatmap showing significantly altered microglial genes by WBRT, but not changed with CSF-1Ri treatment. **c** bar graphs summarizing fold enrichment and p values of the top 20 enriched Biological Processes by Gene Ontology analysis from up-regulated microglial genes after WBRT (full list in

Supplementary Table1). No significantly enriched terms were identified by GO analysis from down-regulated genes by WBRT. **d** a pie chart summarizing all enriched GOBP terms. ns= not significant, ***p<0.0001. **e** scatter plots showing gating strategy in flowsynaptometry analyses. Fluorescent beads at various sizes were used as standard to gate isolated hippocampal cell membrane fractions. Particles between 1 µm and 3 µm were considered synaptosomes and used to determine Synapsin1 and PSD95 protein levels by mean fluorescent intensities (MFIs). **f** dot plots to compare Synapsin1 and PSD95 MFI levels in hippocampal cell fractions. Statistical analyses were performed using two-way ANOVA with Tukey's multiple comparisons test. ns = not significant, *p<0.05, ***p<0.001. N=6.

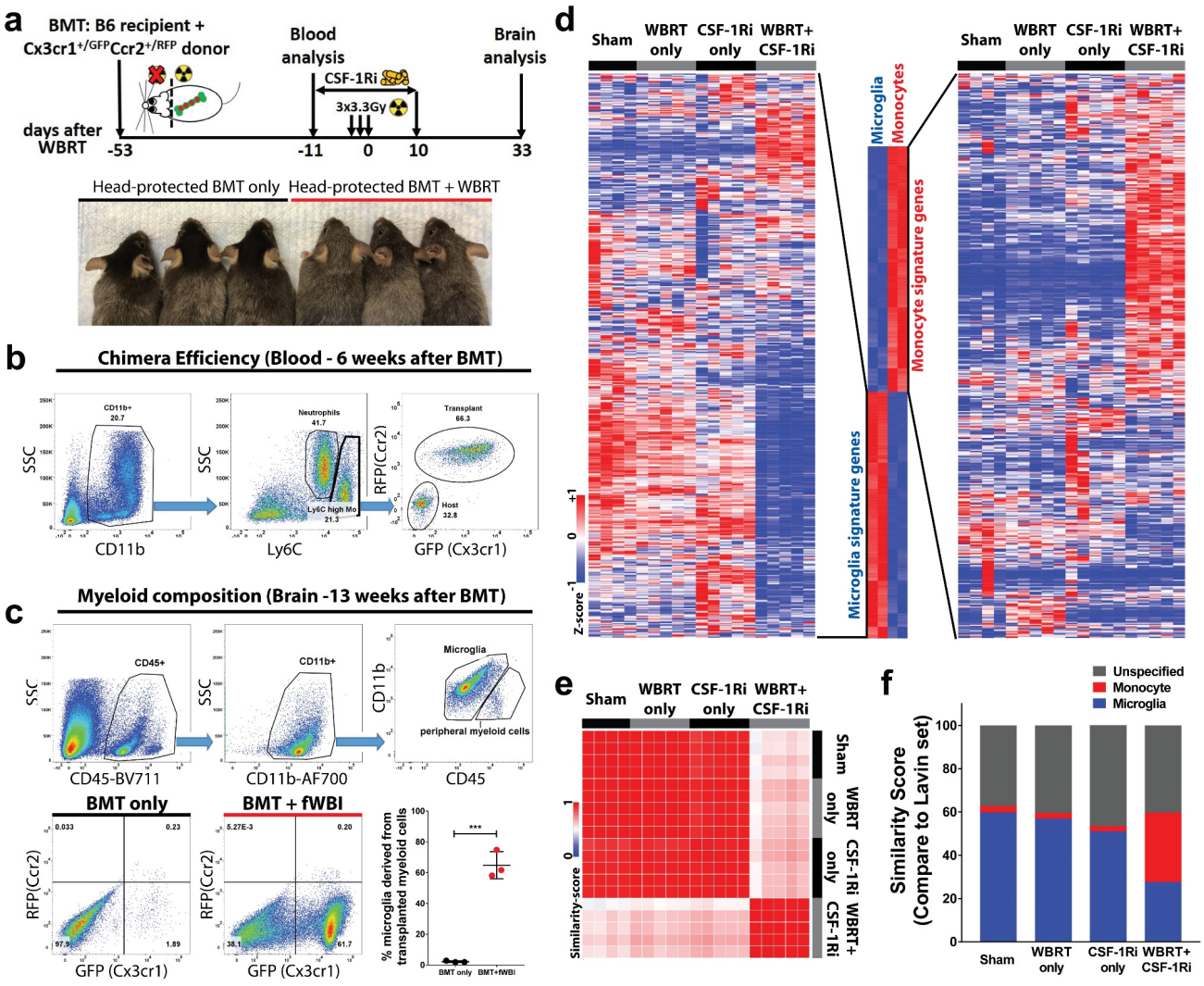

738 **Figure 2: Repopulated microglia-like cells after depletion and WBRT originate from**
739 **peripheral monocytes and retain monocytic signatures. a** experimental design of head-
740 protected bone marrow transplantation (BMT) followed by CSF-1Ri-mediated microglia depletion
741 and WBRT. Lower panel shows fur colors before euthanasian for brain analysis. **b** representative
742 FACS analysis gating strategy to analyze bone marrow chimera efficiency 6 weeks after BMT,
743 about two thirds of the $CD11b^{+}Ly6C^{high}$ monocytes are replaced by $GFP^{+}RFP^{+}$ cells derived from
744 donor bone marrow cells. **c** representative FACS analysis gating strategy and brain myeloid
745 composition results. Upper panel shows FACS gating using CD45 and CD11b staining; microglia
746 and microglia-like cells are defined by positive CD11b staining and low or intermediate CD45
747 levels. Lower panel shows scatter plots of GFP/RFP fluorescent levels of the
748 $CD11b^{+}CD45^{low/intermediate}$ population in the brain, and a dot plot comparing percentages of
749 peripheral myeloid cell derived microglia-like cells. Statistical analysis was performed using
750 unpaired t-test, ***$p<0.001$. **d** hierarchically clustered heatmaps to compare microglia and
751 monocyte signatures. A signature gene list was defined using a dataset published by Lavin and
752 Winter et al, GSE63340. Defined list and expression details are in Supplementary Table 2). **e**
753 Similarity matrix comparisons using defined monocyte and microglia signature genes. **f** bar graph
754 showing similarity scores to compare relative numbers of genes (in percentage of the defined list)
755 that express in the same trends as monocytes or microglia based on the Lavin and Winter *et al*
756 dataset.

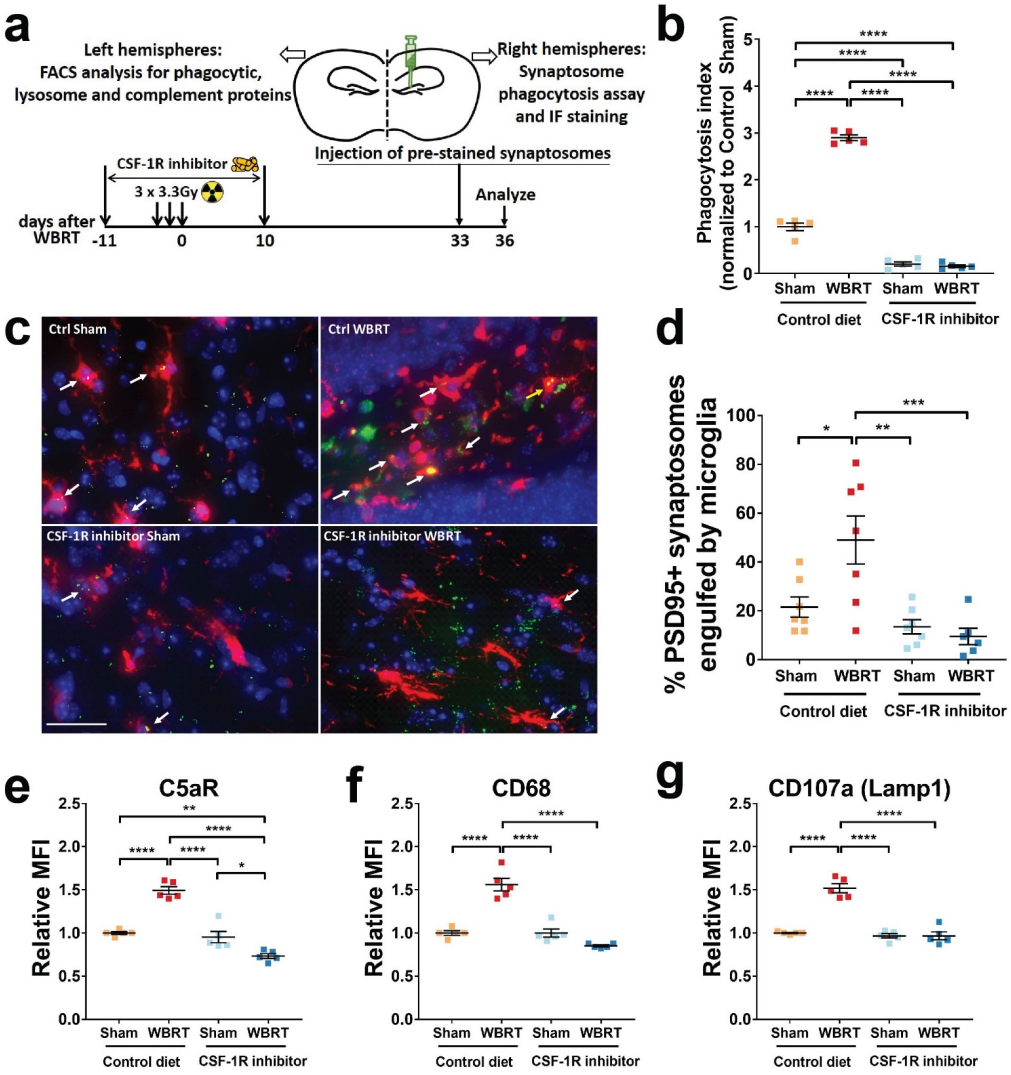

Figure 3: Repopulated microglia and brain-engrafted macrophages are not activated and phagocyte less synaptic compartments. a experimental design for in vivo synaptosome phagocytosis assays. Injection of pre-stained synaptosomes was timed to be the same as previous experiments. Three days later, on day 36 after WBRT, ipsilateral hemispheres were harvested and used for engulfment measurement using FACS or Immunofluorescent staining. **b** FACS analysis result showing levels of microglia that engulfed pre-stained PSD-95 signals. **c** representative images showing engulfment of pre-stained synaptosomes by microglia near injection site. White arrows point at microglia that have engulfed pre-stained synaptosomes. scale bar = 20 μm. **d** dot plot to show quantification result of synaptosome engulfment by

767 immunofluorescent staining. **e – g** dot plots showing cell surface C5aR, and intracellular CD68
768 and CD107a protein levels in microglia and BEMs. Statistical analyses were performed using two-
769 way ANOVA with Tukey's multiple comparisons test. *p<0.05, **p<0.01, ***p<0.001, ****p<0.0001.
770 N = 5 – 6.

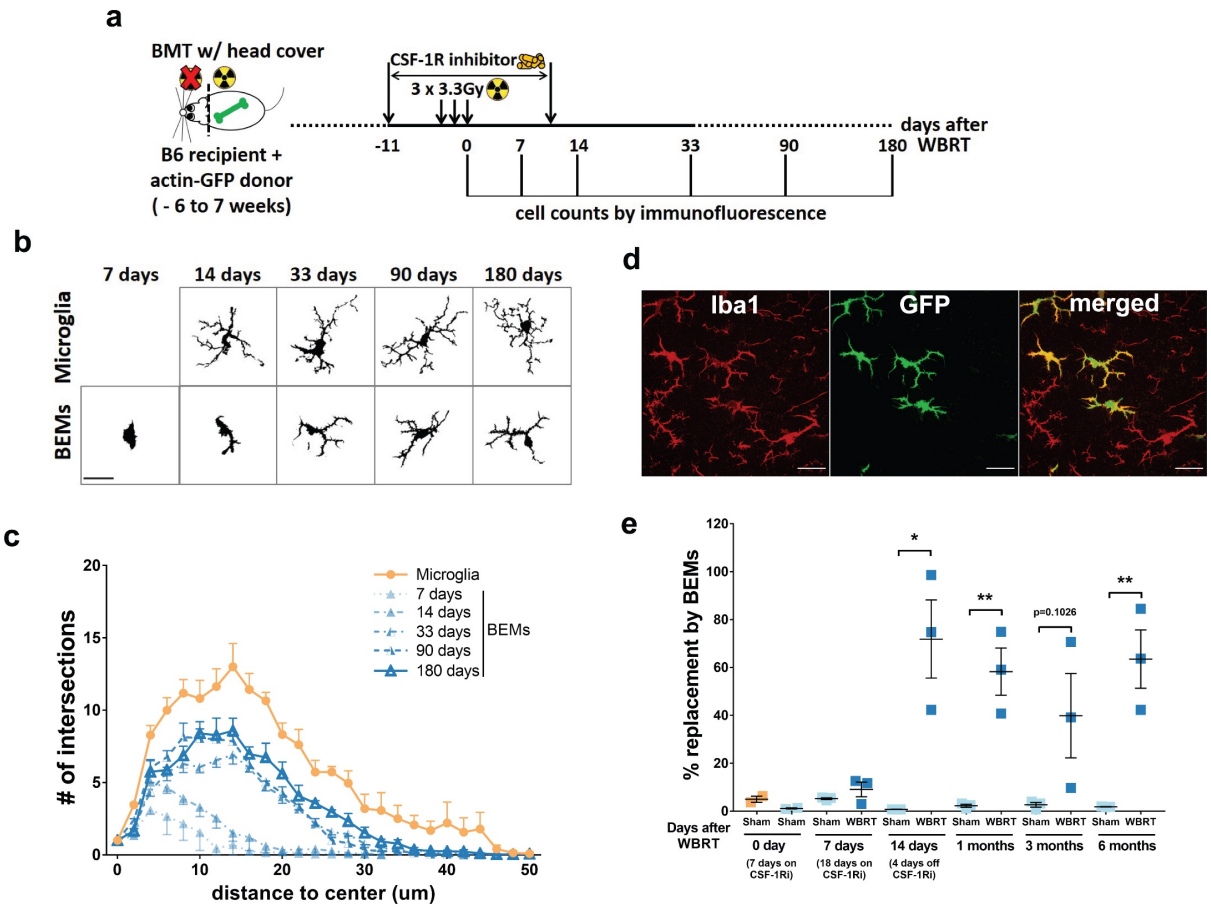

771

772 **Figure 4: BEMs gradually adapt to microglia-like morphology and persist in the brain. a,**
773 schematic of experimental design for long-term assessment of BEMs. **b,** representative images
774 of microglia/BEMs counting, scale bar = 20 µm. **c**, Sholl analysis results showing numbers of
775 intersections at different distances to cell center, BEMs at 7, 14, 33, 90 and 180 days after WBRT
776 were compared to naïve microglia age-matched to 90 days after WBRT., representative images
777 showing differential Iba1 and GFP expressing bprofiles of microglia (Iba1+ GFP-) and BEMs
778 (Iba1+ GFP+) in a BEM bearing brain at 33 days after WBRT. **e**, dot plot to show percentage of

replacement of microglia by BEMs, each dot represent an individual mouse. n = 2 - 3. Statistical analyses were performed using unpaired t-test at each distance point (c) or time point (e). See Supplementary Figure 7 for detailed comparisons between microglia and BEMs at each time point.

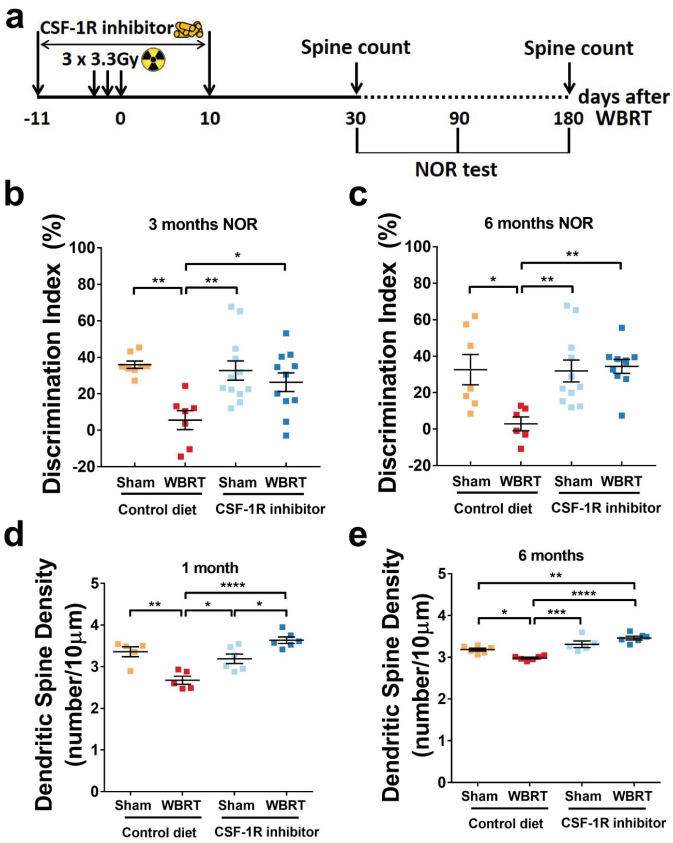

Figure 5: BEMs provide long-term protection against WBRT-induced dendritic spine and memory loss. a schematic of experimental design for long-term memory and dendritic spine density analyses. **b** and **c** dot plots to show NOR test results at 3 and 6 months after WBRT, respectively. N = 6–12. **d** dendritic spine counts of hippocampal granule neurons at 1 month after WBRT (figure reproduced using our previously published data Feng et al[53]). **e** dendritic spine counts of hippocampal granule neurons at 6 months after WBRT, N = 5 – 6.. Statistical analyses were performed using unpaired t-test for each time point (**c**) or two-way ANOVA with Tukey's multiple comparisons test (**e** - **h**). *p<0.05, **p<0.01, ***p<0.001, ****p<0.0001.

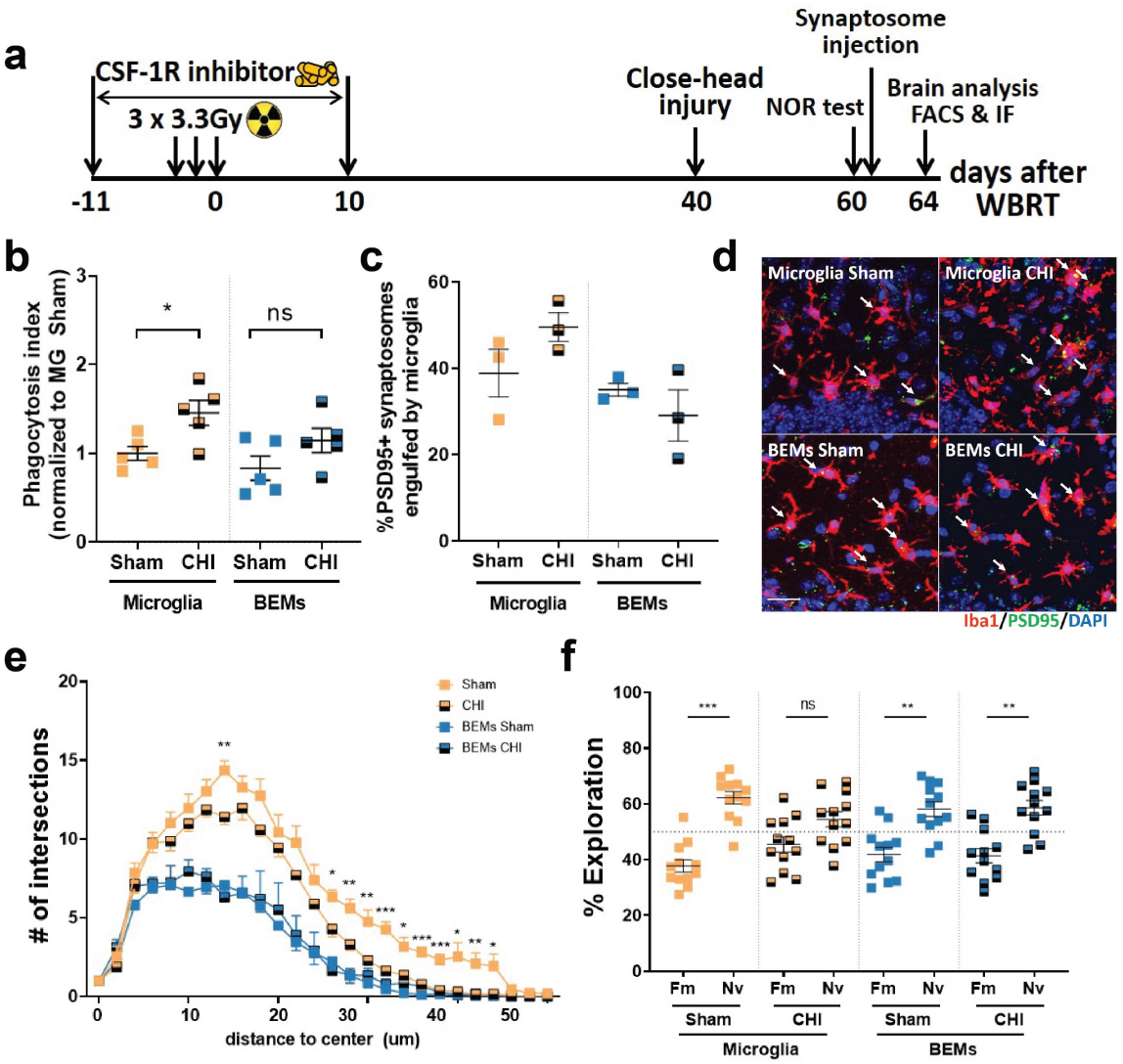

Figure 6: BEMs protects against concussive injury-induced memory deficits. a, schematic of experimental design for concussive injury, cognitive test and following analyses. b, dot plot to show the result of in vivo phagocytosis assay by FACS after injection of pre-stained synaptosomes, each dot represents value from an individual mouse, n = 4 -5. c, dot plot showing result of in vivo phagocytosis assay by IF imaging and quantification, each dot represents mean counts from an individual mouse, n = 3. d, representative images showing microglia and BEMs (arrows) phagocyting injected synaptosomes (green dots). e, Sholl analysis result showing numbers of intersections at different distances to the cell center, n = 5 - 6. f, dot plot showing NOR test result, each dot represent the performance of an individual mouse, n = 12. Statistical analyses

801 were performed using two-way ANOVA with Tukey's multiple comparisons test (b and c) for each

802 distance point (e) or unpaired t-test (f). *$p<0.05$, **$p<0.01$, ***$p<0.001$.

803

804

805